The role of municipal solid waste incineration fly ash in sustainable cementitious system: A waste-derived alkaline activator

Citation for the original published paper (version of record):
Zhang, J., Li, Y., Wang, Y. et al (2025). The role of municipal solid waste incineration fly ash in sustainable cementitious system: A
waste-derived alkaline activator. Case Studies in Construction Materials, 23.
http://dx.doi.org/10.1016/j.cscm.2025.e05264

Case Studies in Construction Materials 23 (2025) e05264

Contents lists available at ScienceDirect

Case Studies in Construction Materials

journal homepage: www.elsevier.com/locate/cscm

The role of municipal solid waste incineration fly ash in sustainable cementitious system: A waste-derived alkaline activator

Junjie Zhang [a,b], Yuzhe Li [a], Yanru Wang [c], Yubin Cao [c,*], Baodong Li [d,*], Arezou Babaahmadi [d], Hao Wang [e]

[a] *School of Materials Science and Engineering, Xi'an University of Architecture & Technology, Xi'an 710055, China*
[b] *State Key Laboratory of Silicate Materials for Architectures, Wuhan University of Technology, Wuhan 430070, China*
[c] *Department of Civil Engineering, Qingdao University of Technology, Qingdao 266033, China*
[d] *Department of Architecture and Civil Engineering, Chalmers University of Technology, Gothenburg 41296, Sweden*
[e] *Centre for Future Materials, University of Southern Queensland, Toowoomba, QLD 4350, Australia*

ARTICLE INFO

Keywords:
MSWIFA
Activation process
Ettringite
Friedel's salt
Heavy metals

ABSTRACT

Municipal solid waste incineration fly ash (MSWIFA) presents both an environmental hazard and an opportunity for sustainable valorization. However, the inherent high alkalinity of MSWIFA is often overlooked in traditional disposal methods. This study investigates the potential of MSWIFA as a fully waste-derived alkaline activator in a sustainable cementitious system. A binary system incorporating 20 wt% MSWIFA and 80 wt% granulated blast furnace slag (GBFS) achieved a 28-day compressive strength of 36.4 MPa, without the conventional chemical activators. The elevated pH provided by MSWIFA effectively triggered GBFS dissolution and promoted the formation of key hydration products, including calcium (alumino) silicate hydrate (C-(A)-S-H), ettringite, and Friedel's salt. Notably, MSWIFA contributed not only to mechanical performance through sustained C-(A)-S-H gel accumulation, but also to environmental performance by enabling in situ immobilization of heavy metals through hydroxide precipitation and encapsulation. Higher MSWIFA dosages enhanced early hydration kinetics and promoted ettringite crystallization, yet reduced Friedel's salt formation due to competitive ion interactions and increased porosity caused by MSWIFA particle morphology. Leaching tests confirmed that all heavy metal concentrations remained well below regulatory thresholds. These findings highlight the potential of MSWIFA as a sustainable, multifunctional activator, offering both chemical reactivity and environmental stabilization in alkali-activated materials. This approach not only valorizes incineration residues but also reduces reliance on commercial alkaline reagents, aligning with circular economic principles.

1. Introduction

Municipal solid waste incineration fly ash (MSWIFA) is a byproduct generated during the incineration of municipal solid waste, with global production projected to reach 0.37–0.44 billion tons annually by 2050 [1–3]. Due to its high content of heavy metals,

---

* Corresponding authors.
E-mail addresses: caoyubin@qut.edu.cn (Y. Cao), baodong.li@chalmers.se (B. Li).

https://doi.org/10.1016/j.cscm.2025.e05264
Received 29 May 2025; Received in revised form 17 August 2025; Accepted 2 September 2025
Available online 4 September 2025

MSWIFA is classified as a hazardous solid waste, and its disposal has become a critical global environmental challenge [4–6]. The landfills of MSWIFA depict high costs, tight land supply and public resistance. The treatment methods for MSWIFA include sintering, water washing, and stabilization/solidification (S/S). Numerous studies attempted to valorize MSWIFA through sintering, water washing, and stabilization/solidification, or to manufacture high value-added products such as glassy ceramics, aggregates, geopolymer or supplementary cementitious materials [7–9]. However, considering the high levels of content and leaching concentration of heavy metals in MSWIFA, the management protocol of MSWIFA should satisfy the requirements of a low volume addition rate and low leachability.

In recent years, the variolization of MSWIFA via alkaline chemicals like NaOH and Na_2SiO_3 as alkali-activated materials (AAMs) has garnered increasing attention as a sustainable disposal strategy [10–12]. Research indicates that the compressive strength of alkali-activated MSWIFA can reach 12.6 MPa at 28 d, while the leaching concentrations of heavy metals remain below the thresholds outlined in relevant standards. To further enhance mechanical properties, researchers have explored incorporating other solid waste streams as precursors in AAM systems [13]. For instance, the incorporation of fly ash (FA), silica fume, and granulated blast furnace slag (GBFS) into alkali-activated MSWIFA systems results in compressive strength improvements of 31.0 %, 47.6 %, and 50.8 % at 28 d, respectively [14].

However, the inherent high alkalinity of MSWIFA is often overlooked in traditional disposal methods. Recent studies suggest that MSWIFA could serve as an activator rather than a precursor for AAM preparation [15–18]. For instance, MSWIFA-activated GBFS, prepared through compression molding, exhibits a compressive strength of up to 34.0 MPa at 28 d [19]. While studies on MSWIFA-activated GBFS-FA systems report compressive strengths of 25.7 MPa at 28 d [20]. In the GBFS case, the alkali content of MSWIFA accelerates the depolymerization and repolymerization processes in GBFS, promoting the formation of hydration products such as C-(A)-S-H, ettringite, and Friedel's salt [21,22]. Simultaneously, compared to traditional alkaline activators such as sodium hydroxide (NaOH) and sodium silicate (Na_2SiO_3), the use of MSWIFA as an alkaline activator achieves substantial reductions in both CO_2 emissions and economic costs [23]. However, the specific mechanisms underlying the activation of GBFS by MSWIFA remain unclear, particularly regarding the formation of hydration products and the evolution of the microstructure. Using MSWIFA as an activator poses an unknown environmental risk. The utilization of MSWIFA as an alkaline activator holds promise not only for developing novel AAMs, but also enables the safe disposal of MSWIFA.

This study explores the potential of using MSWIFA as a sustainable alkaline activator, focusing on the activation mechanism, mechanical properties, and environmental safety. The setting time, compressive strength, drying shrinkage, and pH value are measured, while the activation process is characterized using hydration heat analysis, X-ray diffraction (XRD), thermogravimetric analysis (TGA), and Fourier-transform infrared spectroscopy (FTIR). Microstructural analysis is conducted via mercury intrusion porosimetry (MIP) and scanning electron microscopy (SEM). Furthermore, the environmental safety of the system is evaluated through the leaching behavior of heavy metals and chloride ions. The findings of this study provide valuable insights into the utilization of MSWIFA and offer a design methodology for the development of novel AAMs based entirely on solid waste.

2. Materials and methods

2.1. Materials

In this study, MSWIFA (Xi'an, China) is used as the activator for GBFS (Zhengzhou, China). The chemical compositions and concentrations of heavy metals in both MSWIFA and GBFS are presented in Table 1 and Table 2, respectively. As illustrated in Fig. 1, the primary oxide constituents of these raw materials are CaO, SiO_2, Al_2O_3, and MgO, while MSWIFA exhibits relatively higher levels of Na_2O, K_2O, and Cl. Moreover, as a hazardous waste, MSWIFA contains various heavy metals, including Zn, Ba, Pb, Cu, and Cr. Particle size distribution analysis reveals that the D_{50} of MSWIFA and GBFS is 22.4 μm and 9.3 μm, respectively. The absence of recognizable crystalline phases in GBFS indicates that it is predominantly amorphous. In contrast, MSWIFA contains crystalline phases such as sylvite (KCl), halite (NaCl), calcite ($CaCO_3$), quartz (SiO_2), gypsum ($CaSO_4$), and portlandite ($Ca(OH)_2$). The unignorable presence of $Ca(OH)_2$ contributes to the high pH value of MSWIFA (solid/water ratio 1:10), measured at 12.40, which is capable of activating GBFS [24].

2.2. The preparation of MSWIFA-activated GBFS system

The MSWIFA content was varied between 10 % and 30 % by the weight of GBFS (respectively named as MG10, MG15, MG20, MG25, and MG30). Based on our previous studies, a fixed water-to-binder ratio of 0.3 was selected [25]. The specimen preparation procedure was as follows: (i) MSWIFA and GBFS were mixed at low speed for 2 min, (ii) water was added, and the mixture was stirred at low speed for 2 min, followed by high-speed mixing for an additional 2 min, (iii) the resulting paste was cast into molds, (iv) after demolding, the specimens were cured under standard conditions (20 ± 1°C, RH > 90 %). Specimens with dimensions of

Table 1
The chemical compositions of MSWIFA and GBFS (wt%).

	CaO	SiO_2	Al_2O_3	MgO	SO_3	Fe_2O_3	Na_2O	K_2O	Cl	TiO_2	P_2O_5	Loss	Others
MSWIFA	30.67	13.82	4.15	4.21	8.38	4.11	7.71	9.06	13.03	1.15	1.84	0.05	1.72
GBFS	38.64	36.93	12.32	7.53	2.14	–	0.03	–	–	0.73	–	1.34	0.34

Table 2
The heavy metal composition content of MSWIFA (wt%).

ZnO	BaO	PbO	CuO	Cr_2O_3	SrO_2	SnO_2	Sb_2O_3	CdO	NiO
0.78	0.27	0.22	0.10	0.07	0.07	0.05	0.04	0.03	0.02

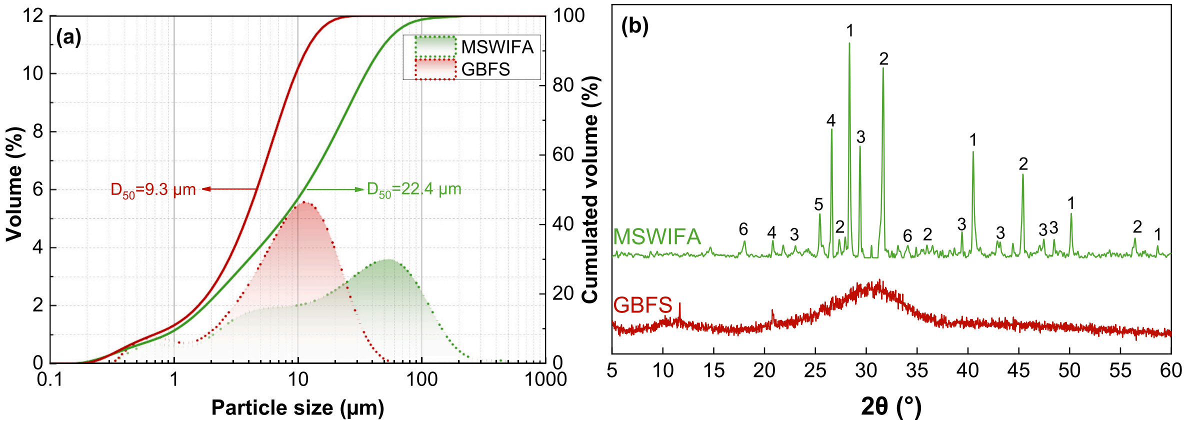

Fig. 1. The basic parameter of raw materials (a) particle size distribution, (b) XRD patterns. 1. PDF# 41–1476 (sylvite), 2. PDF# 05–0628 (halite), 3. PDF# 05–0586 (calcite), 4. PDF# 46–1045 (quartz), 5. PDF# 37–0184 (gypsum), 6. PDF# 04–0733 (portlandite).

40 × 40 × 40 mm^3 were used to evaluate compressive strength, while those measuring 25 × 25 × 280 mm^3 were employed to assess drying shrinkage [26]. Three parallel samples were prepared for each mix, with the error bars serving as indicators of the reproducibility of the test results. After curing, the pastes were immersed in anhydrous ethanol to halt hydration. The pastes were then broken into small particles and ground into powder. Particles smaller than 3 mm were utilized for microstructural and environmental safety evaluations, while the powder passing through a 45 μm sieve was used for analyzing hydration products.

2.3. Methods

2.3.1. Macro-performance

The macro-performance of the binary system is reflected by setting time, compressive strength, drying shrinkage, and pH value. The test of setting time follows the Chinese standard GB/T 1346–2011. The measurement of compressive strength is in line with the Chinese standard GB/T 17671–2021, and the test age is designed as 7 d, 28 d, and 56 d. The analysis of drying shrinkage follows the Chinese standard JC/T 603–2004, and the test starts at 7 d and continues to 90 d. The pH value test is as follows: the mixture of one part powder and ten parts water is magnetically stirred at 400 rpm for 360 min, the leaching solution is obtained, and the pH value is tested by a pH meter (PHS-3C, Leici, China) with a definition of 0.01 [27].

2.3.2. Hydration heat

The hydration heat of the binary system is tested by an isothermal calorimeter (TA, USA). The paste mixing is consistent with Table 3, and approx. 5.0 g pastes are used for the experiment. The data is recorded for up to 168 h.

2.3.3. Hydration products

The hydration products of the binary system are researched by XRD, TGA, and FTIR. XRD (D8 advance, Bruker, German) is used to analyze the crystal phases of hardened pastes. Patterns are collected with Cu (K_α) radiation, with a speed of 4°/min and a step of 0.02°, and the 2θ range is 5–60°. TGA (TGA-1, Mettler, Switzerland) is used to observe the weight loss process of hardened pastes. The temperature range is from room temperature to 1000 °C, with a heating rate of 10 °C/min under the N_2 atmosphere [28]. FT-IR (Nicolet iS20, Thermo Fisher Scientific, USA) is used to research the functional groups of hardened pastes, and the wavenumber

Table 3
The mix-design of the binary system.

ID	MSWIFA	GBFS	Water
MG10	10	90	30
MG15	15	85	30
MG20	20	80	30
MG25	25	75	30
MG30	30	70	30

range is 400–400 cm^{-1}.

2.3.4. Microstructure

The microstructure of the binary system is studied by MIP and SEM. MIP (AutoPore IV 9510, Micromeritics, USA) is used to analyze the pore structure of the hardened pastes. SEM (sigma300, ZEISS, German) is used to observe the morphology of the hardened pastes.

2.3.5. Environmental risk assessment

The environmental safety of the binary system is assessed mainly in terms of chloride ions and heavy metals leaching behavior. The free chloride ions content is tested according to SL/T 352–2020, and the total chloride ions content is calculated based on XRF results (Table 1) [29]. The leachate used for the heavy metal concentration test is prepared by TCLP. Briefly, immerse the dried specimen with the size lower than 3 mm in an acetic acid-based extractant (pH=2.88 ± 0.05) and shake for 20 h with a solid to liquid ratio of 1:20; the leachate is obtained by removing solid particles using 0.45 μm filter membrane; the heavy metal concentration of leachate is measured by the inductively coupled plasma mass spectrometry (ICP-MS, PerkinElmer 8300, USA) [30,31].

3. Results and discussion

3.1. Macro-performance

The macro-performance of the binary system is shown in Fig. 2. As shown in Fig. 2 (a), with the increase in MSWIFA content, the setting process is prolonged. For instance, the initial and final setting times of MG10 are approximately 10 h and 16 h, whereas for MG30, these times are increased to near 33 h and 54 h, respectively. Moreover, the interval between the initial setting and the final setting times also lengthens with increasing MSWIFA content, from 6 h for MG10 to 21 h for MG30. Generally, the initial setting time of OPC is no less than 45 min, and the final setting time of OPC is no more than 390 min, according to the Chinese standard GB 175–2023. In comparison, GBFS activated by strong alkalis like NaOH and Na_2SiO_3, the initial and final setting time is no more than 1 h and 2 h, respectively [32]. By contrast, the setting process for the MSWIFA-activated GBFS system is significantly slower.

The compressive strength of the binary system is shown in Fig. 2(b). It is observed that compressive strength improves with increasing MSWIFA content, with an optimal strength recorded at MG20. Beyond 20 % MSWIFA, the strength decreases. For instance, the 28d compressive strength of MG10, MG20, and MG30 is 28.6 MPa, 36.4 MPa, and 26.5 MPa, respectively. Additionally, compressive strength increases progressively over time, displaying a similar trend to OPC. The compressive strength of MG20, for example, rises from 27.2 MPa at 7 d to 36.4 MPa at 28 d and 44.0 MPa at 56 d. These results suggest that the compressive strength of the MSWIFA-activated GBFS system is largely influenced by MSWIFA content. Moreover, the continuous development of strength supports the potential of this system as a novel cementitious material. Inactivated GBFS typically exhibits low reactivity and negligible

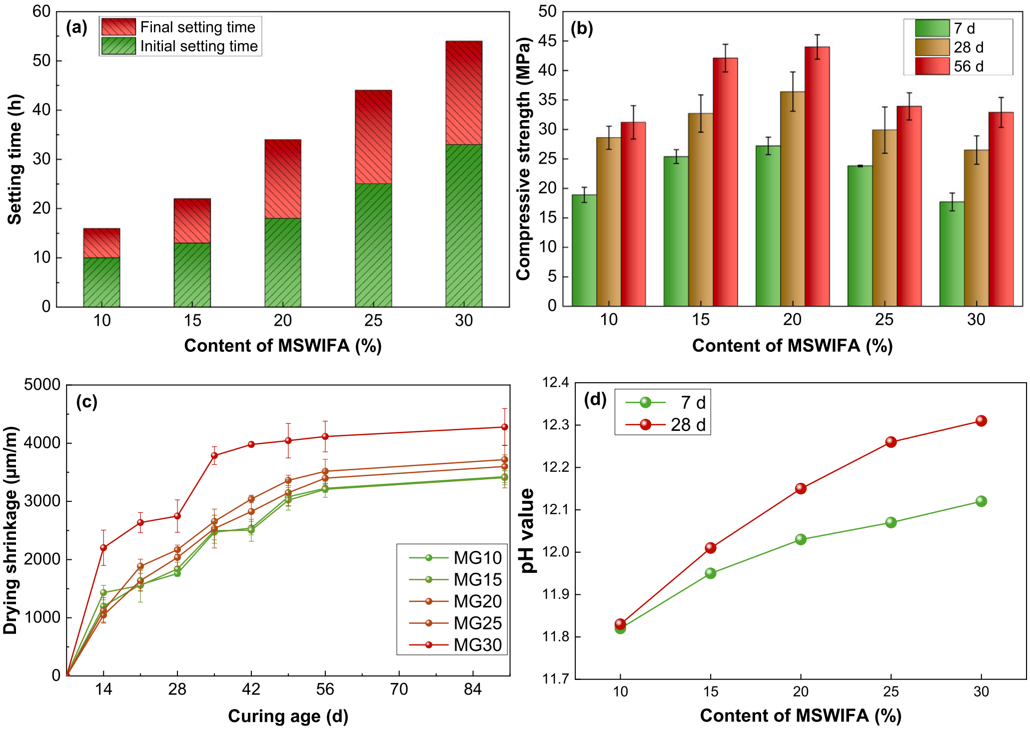

Fig. 2. The macro-performance of MSWIFA-activated GBFS system (a) setting time, (b) compressive strength, (c) drying shrinkage, (d) pH value.

mechanical properties, whereas MSWIFA activation significantly enhances the mechanical performance of GBFS in this study [33].

The drying shrinkage behavior of the binary system is presented in Fig. 2(c). Drying shrinkage increases progressively over time, primarily due to the loss of free water in the hardened pastes under controlled conditions (20 ± 3°C, RH = 50 ± 4 %). The most rapid shrinkage occurs within the first 56 d, after which the rate of shrinkage diminishes. Shrinkage also increases with higher MSWIFA content, with MG30 exhibiting the most pronounced shrinkage at all curing ages. Shrinkage is influenced by both the formation of hydration products and the microstructural compactness. C-(A)-S-H contributes to shrinkage, while ettringite induces expansion [34]. A denser microstructure can reduce the free water loss, resulting in lower shrinkage. In this case, it is inferred that the drying shrinkage behavior of the MSWIFA-activated GBFS system is dependent on the compactness of the microstructure and the type of hydration products.

The pH values of the binary system, as shown in Fig. 2(d), increase with rising MSWIFA content, regardless of curing age. MSWIFA and GBFS exhibit pH values of 12.40 and 9.54, respectively, significantly influencing the pH of the system. The pH value also increases slightly over time. For instance, the pH of MG20 increases from 12.03 at 7 d to 12.15 at 28 d. This aligns with previous findings [35–37], which suggest that as GBFS undergoes self-hydration, its alkalinity increases over time due to the consumption of dissolved calcium ions for C-(A)-S-H formation. This process similarly occurs the MSWIFA-activated GBFS system.

In summary, the MSWIFA-activated GBFS system exhibits a slow setting process, continuously improving compressive strength, and increasing pH values over time. With a compressive strength of 36.4 MPa at 28 d for a 20 % MSWIFA-80 % GBFS blend, this system shows promise as a novel cementitious material derived entirely from solid waste.

3.2. Hydration heat

The hydration heat of the binary system is shown in Fig. 3. MSWIFA significantly alters the hydration behavior of GBFS. As illustrated in Fig. 3(a), the hydration process can be divided into five stages, resembling the typical hydration process of OPC. The first stage (pre-induction period) results from the rapid dissolution of minerals and amorphous phases in the raw materials. The second stage (induction period) is associated with the precipitation-dissolution equilibrium of hydration products. The third and fourth

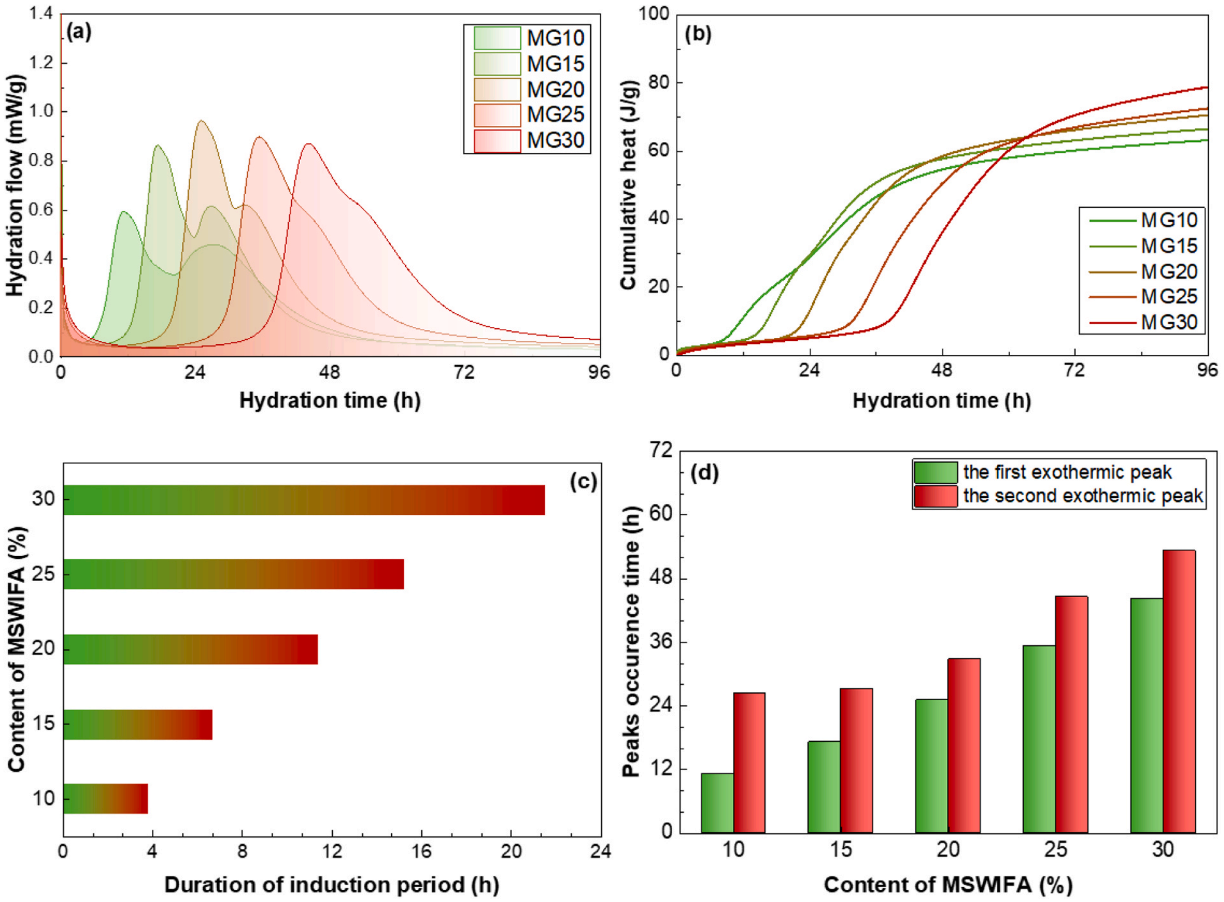

Fig. 3. The hydration heat of MSWIFA-activated GBFS system (a) hydration flow, (b) cumulative heat, (c) duration of induction period, (d) peaks occurrence time.

stages—acceleration and deceleration periods—are characterized by the rapid formation and accumulation of hydration products. Notably, the hydration flow curve of the binary system exhibits two distinct exothermic peaks. The first peak is primarily attributed to the rapid formation of ettringite, while the second peak is linked to the formation of Friedel's salt [21]. The final stage (decline period) indicates that ongoing hydration continues in the system.

The cumulative heat evolution of the binary system is shown in Fig. 3(b). In the early stages, cumulative heat decreases with increasing MSWIFA content. However, over time, groups with higher MSWIFA content generate more heat compared to those with lower content. By the later stages, cumulative heat increases proportionally with higher MSWIFA content. For example, at 72 h, the cumulative heats for MG10, MG20, and MG30 are 60.2, 66.3, and 70.6 J/g, respectively. This cumulative heat indicates the degree of GBFS activation by MSWIFA—the greater the cumulative heat, the more hydration products are formed. Thus, GBFS with lower MSWIFA content exhibits a short induction period but limited hydration, while GBFS with higher MSWIFA content shows a prolonged induction period, allowing for more extensive hydration.

The duration of the induction period is shown in Fig. 3(c) and is extended with increasing MSWIFA content. The induction periods for MG10, MG20, and MG30 are 3.8 h, 11.4 h, and 21.5 h, respectively. Heavy metals such as Zn^{2+} and Pb^{2+} in MSWIFA react with OH^- ions from GBFS dissolution, forming hydroxides that coat the surface of GBFS particles, inhibiting dissolution and delaying hydration [38]. As the alkalinity of the pore solution increases, this retarding effect diminishes, allowing the activation process to resume. Similarly, in OPC, the surface of cement particles is initially covered by ettringite, causing an induction period. In the binary system, ettringite forms due to the reaction between MSWIFA and GBFS, and the precipitation of hydration products is further difficult affected by the complex ionic environment. The absence of nucleating agents, such as nano-SiO_2, also hinders the precipitation process [15]. These factors contribute to the prolonged induction period, which is further extended with higher MSWIFA content as more ettringite forms, increasing the ionic complexity of the environment.

The timing of the exothermic peaks is displayed in Fig. 3(d). The occurrence of exothermic peaks is delayed as MSWIFA content increases. For MG10, MG20, and MG30, the first exothermic peaks appear at 11.3 h, 25.1 h, and 44.2 h, respectively, while the second exothermic peaks occur at 26.5 h, 32.8 h, and 53.3 h, respectively. Additionally, Fig. 3(a) shows that the intensity of the first exothermic peak follows a rise-then-fall trend, with the highest intensity observed in MG20, suggesting that ettringite accumulation occurs most rapidly in this system. However, the second exothermic peak becomes less pronounced as MSWIFA content increases, likely due to the inhibitory effect of ettringite on Friedel's salt formation.

Generally, the MSWIFA-activated GBFS system exhibits a prolonged induction period due to the formation of ettringite and heavy metal precipitation on the GBFS surface. Furthermore, the second exothermic peak diminishes with increasing MSWIFA content, as ettringite suppresses Friedel's salt formation.

3.3. Hydration products

3.3.1. XRD analysis

The XRD patterns of the binary system are displayed in Fig. 4, revealing the crystalline phases present in the hardened pastes at different curing ages. The major crystalline components identified in the system include sylvite (KCl), halite (NaCl), calcite ($CaCO_3$), quartz (SiO_2), ettringite, and hydrocalumite (Friedel's salt). Among these, KCl, NaCl, $CaCO_3$, and SiO_2 are derived from MSWIFA, whereas ettringite and Friedel's salt are primary hydration products of the system.

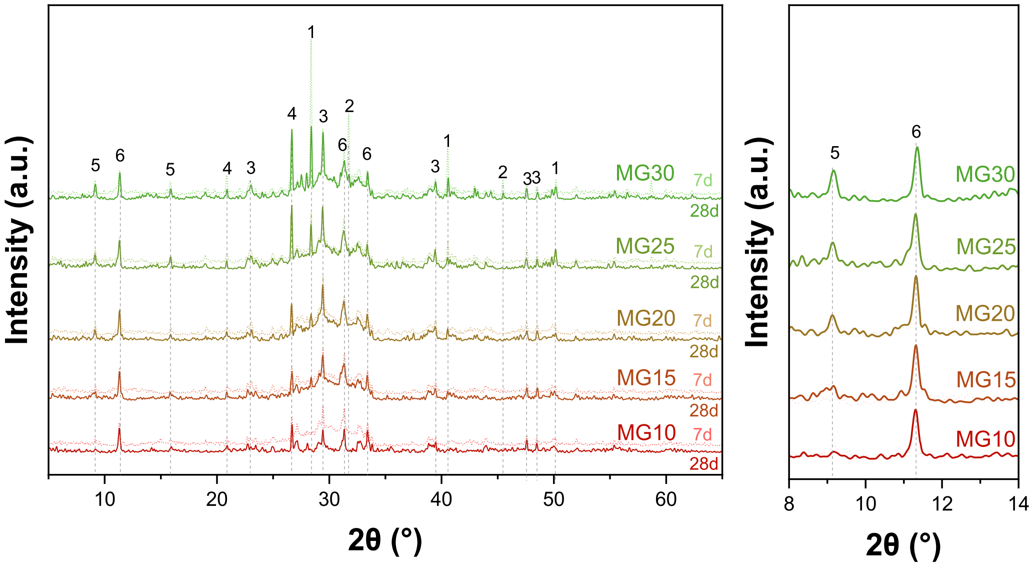

Fig. 4. XRD patterns of MSWIFA-activated GBFS system. 1. PDF# 41–1476 (sylvite), 2. PDF# 05–0628 (halite), 3. PDF# 05–0586 (calcite), 4. PDF# 46–1045 (quartz), 5. PDF# 41–1451 (ettringite), 6. PDF# 19–0202 (hydrocalumite).

At 7 d, the intensity of ettringite peaks increases with the rise in MSWIFA content. This can be attributed to the sulfate ions dissolved from MSWIFA, which react with calcium ions and the aluminum phase in the pore solution, forming ettringite under high alkalinity conditions. As MSWIFA content increases, both the alkalinity and the availability of sulfate ions rise, promoting faster formation and accumulation of ettringite. In contrast, the intensity of hydrocalumite (Friedel's salt) peaks shows a non-linear relationship with MSWIFA content, peaking in the MG20 group. Chloride ions, also derived from MSWIFA, react with calcium and aluminum to form Friedel's salt [4]. However, in systems where both sulfate and chloride ions are present, ettringite is preferentially formed in the early stages. As the available sulfate becomes depleted, Friedel's salt formation is accelerated. For MSWIFA content above 20 %, peaks for KCl and NaCl become more prominent, suggesting that the formation of Friedel's salt is limited by the available aluminum in the system.

At 28 d, the XRD patterns reveal an overall increase in the peak intensities of both ettringite and Friedel's salt, indicating ongoing hydration. However, the increase in Friedel's salt peak intensity is more significant compared to ettringite, as the sulfate ions become exhausted over time, leaving sufficient chloride ions to continue reacting with calcium and aluminum. Notably, the peak intensity of ettringite in the MG10 group decreases from 7 d to 28 d. This is likely due to the instability of ettringite under low pH conditions, as reported in previous studies [39]. Interestingly, the peaks corresponding to KCl and NaCl become less pronounced at 28 d, particularly in the MG10 and MG15 groups. This can be attributed to the continued formation of Friedel's salt, which consumes a substantial portion of the chloride ions present in the system. In contrast, groups with higher MSWIFA content (>20 %) still show significant KCl and NaCl peaks, indicating that the excess chloride ions, in the absence of sufficient aluminum phase, remain unreacted and contribute to the crystalline structure.

3.3.2. TG-DTG analysis

The TG-DTG patterns of the binary system are shown in Fig. 5, illustrating six distinct weight loss peaks during the decomposition process. The peak observed around 90 °C corresponds to the decomposition of C-(A)-S-H and ettringite (AFt), while the peaks near 120 °C and 360 °C are attributed to the decomposition of Friedel's salt. The weight loss peak between 400 and 600 °C represents the decomposition of $Ca(OH)_2$, the peak within the range of 750–850 °C corresponds to the decomposition of $CaCO_3$ and other carbonates, and the peak around 850–970 °C responds to the volatilization of NaCl and KCl [40,41].

At 7 d, the weight loss peak associated with C-(A)-S-H/AFt initially increases and then decreases with rising MSWIFA content, reaching its maximum intensity in the MG20 sample. The variations in peak intensity for Friedel's salt and $Ca(OH)_2$ between the different groups are relatively minor. Additionally, due to the composition of the raw materials, the weight loss peaks corresponding to $CaCO_3$ and NaCl/KCl are significantly enhanced as the MSWIFA content increases. At 28 d, the weight loss peak for C-(A)-S-H/AFt is further intensified with the increase in MSWIFA content, with MG30 showing the highest peak intensity. Compared to the 7 d results, the NaCl/KCl weight loss peak diminishes at 28 d, indicating that chloride ions are being consumed by the formation of Friedel's salt.

The weight loss in the 50–400 °C range, resulting from the decomposition of C-S-H, AFt, and Friedel's salt, increases with the MSWIFA content. The highest weight loss is observed in MG20 at 7 d, whereas MG30 shows the highest loss at 28 d. In the binary system, the initial hydration products are primarily AFt and Friedel's salt. Under sufficient alkaline conditions, calcium ions react with the aluminum-silicon phase in the pore solution to form C-(A)-S-H. In the early stages, AFt and Friedel's salt are the dominant hydration products. However, as the available sulfate and aluminum phases in the pore solution are consumed, the formation of crystalline phases slows. As a result, C-(A)-S-H becomes the predominant hydration product in the later stages. Furthermore, as shown in Fig. 6, the weight loss at 28 d exceeds that observed at 7 d, with MG20's weight loss increasing from 7.43 % at 7 d to 8.06 % at 28 d, which is attributed to the sustained activation of GBFS by MSWIFA. The weight loss in the 600–1000 °C range, primarily due to the decomposition of $CaCO_3$ and NaCl/KCl, increases proportionally with MSWIFA content. However, between 7 d and 28 d, a reduction in weight loss is observed, particularly in the samples with higher MSWIFA content, due to the consumption of chloride ions for the

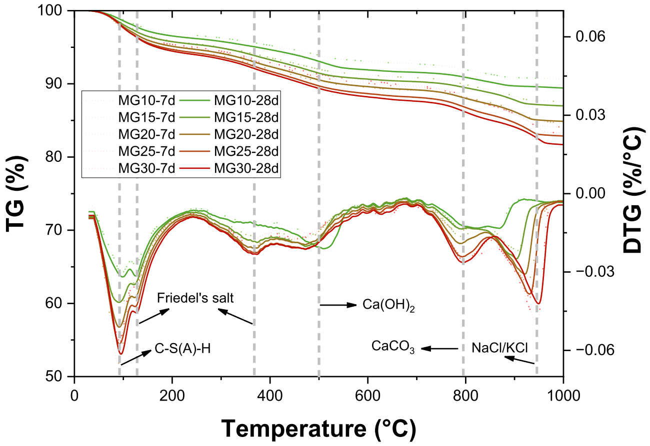

Fig. 5. TG-DTG patterns of MSWIFA-activated GBFS system (a) TG-DTG curves at 7 d, (b) TG-DTG curves at 28 d, (c) weight loss at 50–400 °C, (d) weight loss at 600–1000 °C.

formation of Friedel's salt.

3.3.3. FT-IR analysis

The FT-IR spectra of the binary system are shown in Fig. 7, revealing five distinct absorption peaks. The absorption peak around 3440 cm^{-1} is attributed to the stretching vibration of Al-OH, which is formed due to hydration products such as C-(A)-S-H, ettringite (AFt), and Friedel's salt [41]. The absorption peak at approximately 1630 cm^{-1} corresponds to the bending vibration of H-O-H, originating from the interlayer water within the hydration products. Additionally, the peaks near 1480 cm^{-1} and 870 cm^{-1} are associated with the stretching and bending vibrations of C-O, primarily derived from $CaCO_3$ present in the raw materials [19]. The absorption peak around 970 cm^{-1} is attributed to the stretching vibration of Si(Al)-O in C-(A)-S-H [42].

At 7 d, the absorption peaks near 3440 cm^{-1} and 1630 cm^{-1} intensify with increasing MSWIFA content, suggesting that MSWIFA effectively activates GBFS to produce hydration products. However, a reduction in the absorption peak is observed in the MG30 sample, indicating that during the early stages of hydration, crystals such as AFt and Friedel's salt are the predominant hydration products rather than C-(A)-S-H. The absorption peaks near 970 cm^{-1} and 520 cm^{-1} is also enhanced with rising MSWIFA content, indicating that MSWIFA accelerates the formation of C-(A)-S-H. Furthermore, the absorption peaks around 1480 cm^{-1} and 870 cm^{-1} are amplified as the MSWIFA content increases, which is linked to the elevated amount of $CaCO_3$ in the raw materials. At 28 d, the absorption peaks near 3440 cm^{-1}, 1630 cm^{-1}, and 970 cm^{-1} are further enhanced with increasing MSWIFA content. Over time, as sulfate and chloride ions in the pore solution are consumed, the formation of C-(A)-S-H gradually becomes the dominant hydration product.

In conclusion, the hydration products in the MSWIFA-activated GBFS system primarily include ettringite, Friedel's salt, and C-(A)-S-H. The increase in MSWIFA content facilitates the early formation of hydration products such as ettringite and Friedel's salt, while C-(A)-S-H becomes the primary hydration product at later stages. However, the generation of Friedel's salt is inhibited by the presence of ettringite, particularly at higher MSWIFA contents.

3.4. Microstructure

3.4.1. MIP analysis

The pore structure of the binary system at 28 d is illustrated in Fig. 8. As shown in Fig. 8(a), MSWIFA exerts a significant influence on the most probable aperture. With an increase in MSWIFA content from 10 % to 20 %, the most probable aperture enlarges from 13.7 nm to 17.1 nm. Beyond 20 % MSWIFA content, the most probable aperture bifurcates into two distinct ranges: the first is below 10 nm, and the second is within 20–30 nm. Notably, the second aperture decreases with higher MSWIFA content. At lower MSWIFA content, the voids created by crystals are readily filled by the formation of C-(A)-S-H. However, at higher MSWIFA content, the rapid accumulation of crystals leads to the formation of numerous voids that cannot be filled by C-(A)-S-H. Hence, the first most probable aperture is associated with C-(A)-S-H formation, while the second is linked to the presence of crystals, which enlarge as MSWIFA content increases.

Fig. 8(b) illustrates the porosity and pore area of the binary system. The porosity demonstrates an initial decrease followed by an increase with rising MSWIFA content, with the lowest porosity observed at MG20. Specifically, porosity decreases from 35.9 % in MG10 to 28.2 % in MG20, representing a 21.5 % reduction. This suggests that a lower MSWIFA content significantly reduces porosity, as the addition of MSWIFA effectively activates GBFS, promoting the formation of various hydration products that contribute to microstructure densification. However, as MSWIFA content increases from MG20 to MG30, porosity rises from 28.2 % to 33.8 %, a 19.8 % increase, indicating that excessive MSWIFA content affects development of porosity negatively. This can be attributed, in part, to the larger particle size of MSWIFA compared to GBFS, which limits its filler effect. Additionally, the extended induction period caused by the presence of heavy metals and the activation method hinders the compactness of the microstructure. The trends in pore area and porosity are comparable; for example, the pore areas of MG10, MG20, and MG30 are 65.1 m^2/g, 51.4 m^2/g, and 52.8 m^2/g,

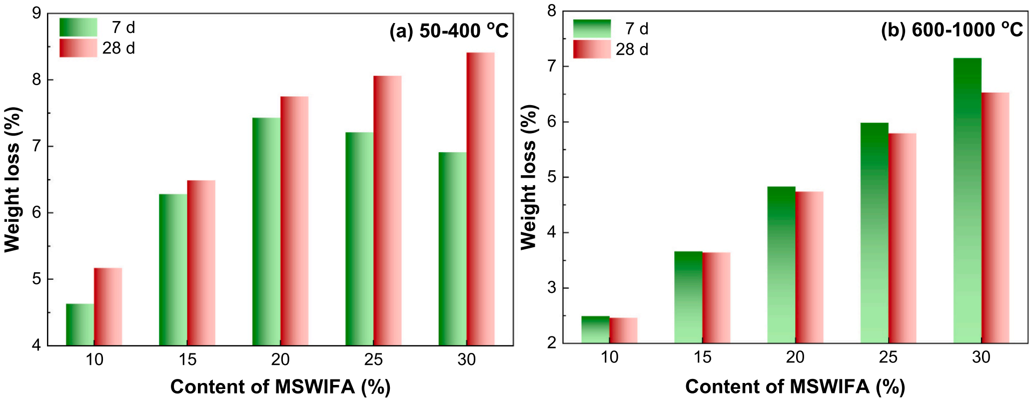

Fig. 6. Mass loss results from TG-DTG, (a) 50–400 °C, (b) 600–1000 °C.

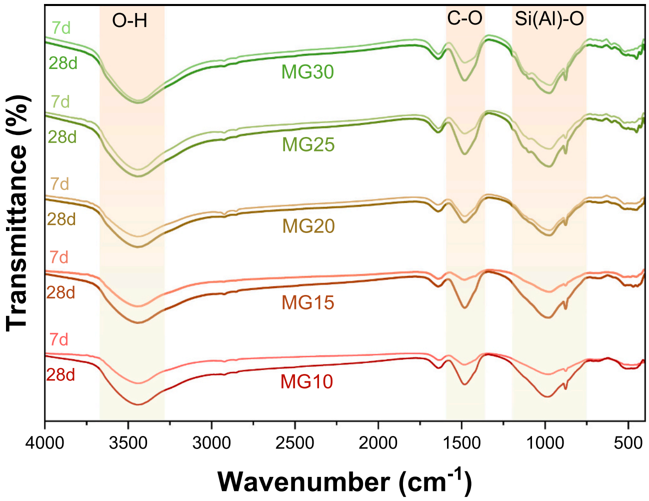

Fig. 7. FT-IR spectra of MSWIFA-activated GBFS system.

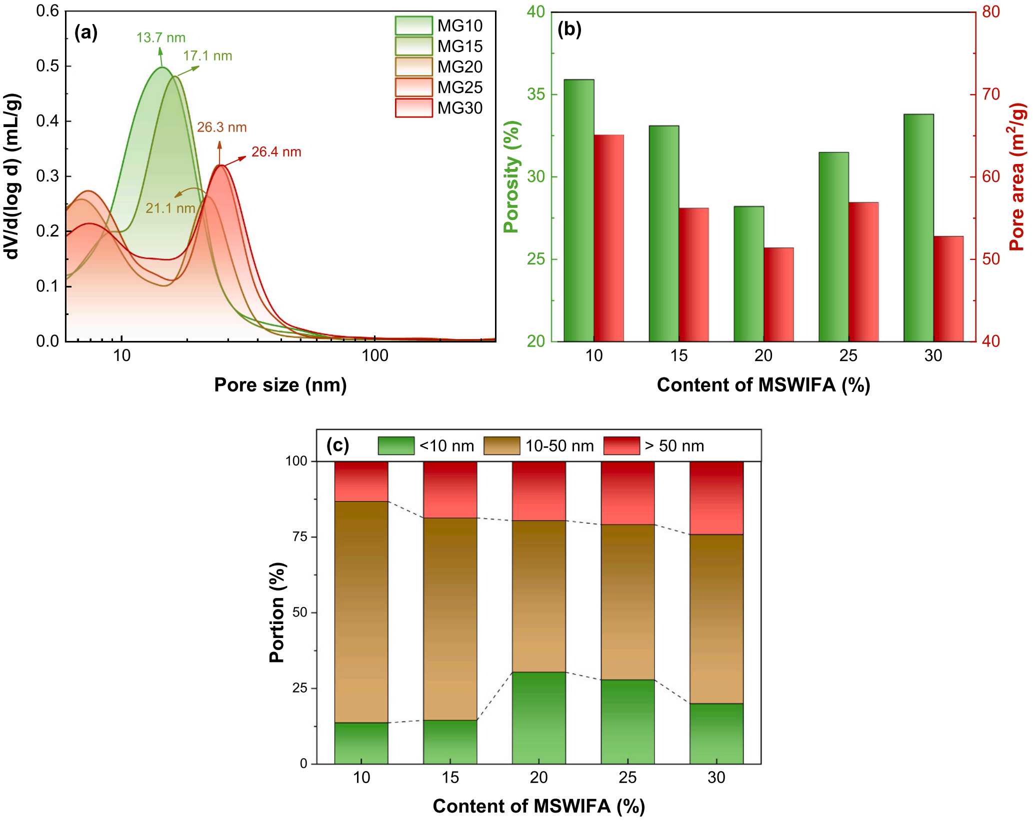

Fig. 8. Pore structure of MSWIFA-activated GBFS system (a) most probable aperture, (b) porosity and pore area, (c) pore volume distribution.

respectively. Moreover, MG30 exhibits a lower pore area than MG25, suggesting that the large pore volume in MG30 is due to a loose microstructure.

The pore volume distribution of the binary system is presented in Fig. 8(c), with pores categorized based on their radius into gel pores (<10 nm), fine capillary pores (10–50 nm), and larger pores (>50 nm) [37]. It is important to note that gel pores are considered harmless, fine capillary pores are nearly harmless, and larger pores are classified as harmful [43–45]. The volume of gel pores increases with the rise in MSWIFA content, indicating that MSWIFA enhances the formation of C-(A)-S-H. The volume of fine capillary pores initially decreases and then increases, reflecting the content and arrangement of crystals. Furthermore, the volume of harmful pores increases with higher MSWIFA content, which is determined by both the composition of the cementitious materials and the distribution of hydration products.

3.4.2. SEM analysis

The SEM images of the binary system are presented in Fig. 9. Hydration of the binary system generated multiple phases: hexagonal plate-shaped Friedel's salt, amorphous C-(A)-S-H gel, and acicular ettringite crystals [46]. As shown in Fig. 9 (a)-(c), at 7 d, layered Friedel's salt is observed to be covered by amorphous C-(A)-S-H across all groups. However, ettringite is only visible in MG30, suggesting that its presence in MG10 and MG20 is likely too low to be directly observed. In MG10, Friedel's salt appears thin and loosely packed, while in MG20, the axial alignment of Friedel's salt becomes more pronounced. In MG30, Friedel's salt is notably thicker but still distributed sparsely, indicating that the morphology of Friedel's salt is influenced by the MSWIFA content. As shown in Fig. 9 (d)-(f), at 28 d, the microstructure's compactness is significantly enhanced compared to 7 d, which is attributed to the continuous activation of GBFS by MSWIFA. Over time, the size and thickness of Friedel's salt increase. In MG20, various hydration products intermix, resulting in a denser microstructure. However, in MG30, the rapid accumulation of crystals during the early stages creates voids, leading to a comparatively looser microstructure in the later stages.

In summary, the microstructure of the MSWIFA-activated GBFS system becomes progressively denser over time due to the accumulation of hydration products, particularly C-(A)-S-H. Nevertheless, the porosity and volume of harmful pores increase as MSWIFA content rises, likely due to the larger particle size introduced by the MSWIFA.

3.5. Environmental safety

Environmental safety is a critical factor in evaluating the feasibility of developing a binary system as a fully solid waste-based cementitious material. The leaching results for the binary system after 28 d are presented in Fig. 10. As depicted in Fig. 10 (a), the leaching concentrations of Cu, Zn, Cd, and Pb in the MG30 group were 9.0 μg/L, 1052.3 μg/L, 68.7 μg/L, and 31.7 μg/L, respectively. These values fall well below the regulatory limits of 120 mg/L, 120 mg/L, 0.6 mg/L, and 1.2 mg/L, as stipulated by Chinese environmental standards [47]. Consequently, the leaching concentrations of all four heavy metals are significantly lower than the permissible thresholds, indicating minimal risk of heavy metal leaching. The hydration products play a key role in immobilizing heavy metals through both physical and chemical mechanisms [42]. Specifically, the C-(A)-S-H phases, which possess a high specific surface area, exhibit considerable adsorption capacity for heavy metal ions. Additionally, heavy metal ions can substitute for other ions within the C-(A)-S-H structure as well as within ettringite [48]. Furthermore, the heavy metals can be encapsulated within the hydration products, further mitigating their mobility and environmental impact [49].

In the highly alkaline conditions of these systems, Al-O and Si-O tetrahedra from MSWIFA are continuously dissolved and react with calcium ions to form C-(A)-S-H, while Al-O tetrahedra transform into Al-O octahedra, facilitating the formation of ettringite and Friedel's salt [50,51]. This process not only enhances mechanical performance but also reduces the leaching of heavy metals and consumes chloride ions through the generation of Friedel's salt [42]. As harmful substances are effectively immobilized through physical encapsulation, adsorption, and chemical reactions, thereby meeting stringent environmental safety requirements [52–54].

The immobilization capacity for chloride ions increases with the rise in MSWIFA content, while the immobilization efficiency decreases. Specifically, the chloride ion immobilization amounts for MG10, MG20, and MG30 are 10.5 mg/g, 17.0 mg/g, and 23.7 mg/g, respectively, with corresponding immobilization rates of 80.8 %, 65.3 %, and 60.6 %. In addition to the strong adsorption

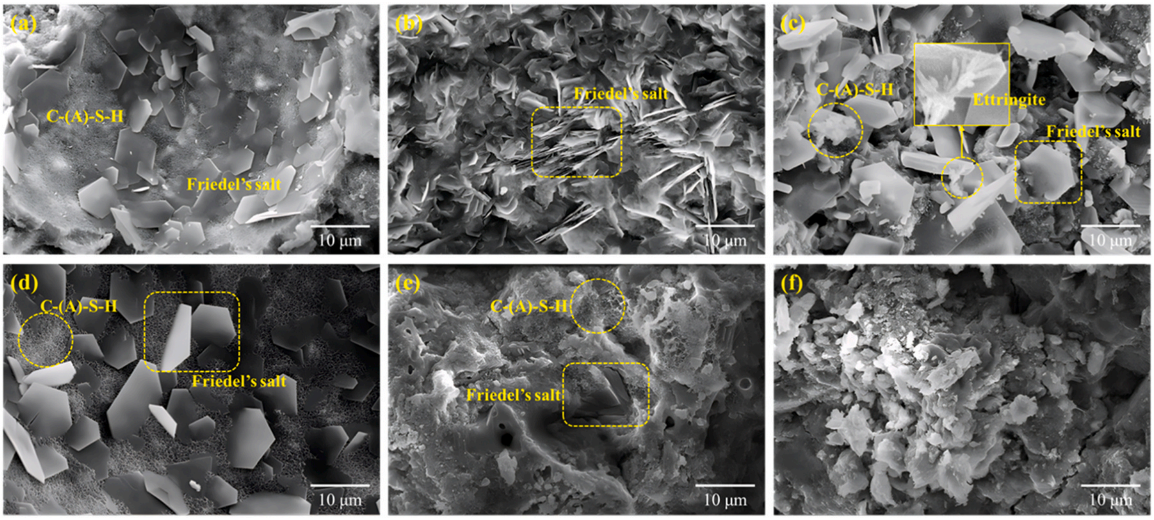

Fig. 9. SEM images of MSWIFA-activated GBFS system (a) MG10 at 7 d, (b) MG20 at 7 d, (c) MG30 at 7d, (d) MG10 at 28 d, (e) MG20 at 28 d, (f) MG30 at 28 d.

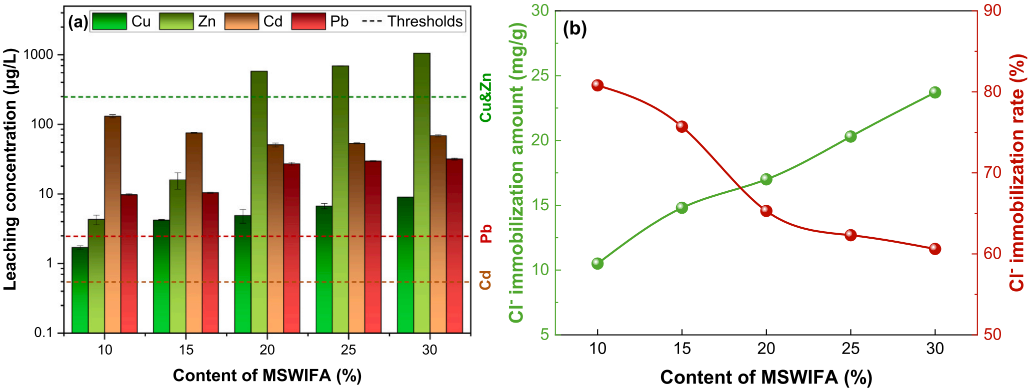

Fig. 10. Leaching behavior of MSWIFA-activated GBFS system, (a) heavy metals, (b) chloride ions.

capacity, chloride ions in the binary system are immobilized through the formation of Friedel's salt [17]. MSWIFA, in its untreated form, contains a high concentration of chloride ions, but due to the limited availability of aluminum phases, the content of Friedel's salt is restricted. As a result, the chloride ion immobilization efficiency in the MSWIFA-activated GBFS system is suboptimal. Despite this, the MSWIFA-activated GBFS system demonstrates considerable environmental safety. Chloride ions are actively involved in the formation of Friedel's salt, while heavy metals are effectively stabilized through precipitation reactions and physical adsorption. The leaching concentrations of heavy metals are well below the permissible limits set by national standards, further underscoring the system's environmental viability.

3.6. Mechanism discussion

In the present research, MSWIFA is used to activate GBFS, with the compressive strength of the MSWIFA-activated GBFS system increasing over time. And the heavy metals leaching concentration of the MSWIFA-activated GBFS system is far lower than the limitation of related national standards, exhibiting great environmental safety. The reaction mechanism of the MSWIFA-activated GBFS binary system is shown in Fig. 11.

In the initial stage, raw materials, including MSWIFA and GBFS, are wet by water, resulting in the dissolution of various ions. The presence of MSWIFA has a significant positive effect on the dissolution process of GBFS. The dissolution of $Ca(OH)_2$ in MSWIFA can increase the pH value of the solution, and the depolymerization process of GBFS is facilitated by that, resulting in the formation of Si-O tetrahedral groups and Al-O tetrahedral groups [55]. Meanwhile, SO_3 present in MSWIFA transforms into sulfate during the hydration process, participating in the reaction to form ettringite [56]. However, the surface of GBFS can be covered by the presence of heavy metal precipitation and ettringite in the early period, and the activation process is significantly retarded, exhibiting a long induction period [15]. In addition, in the case of coexistence of sulfate and chloride ions, the generation of ettringite is favored, and the formation of Friedel's salt is inhibited [21]. In the later period, the sulfate in the pore solution is consumed, and the generation of Friedel's salt is promoted. Meanwhile, the accumulation of C-(A)-S-H is continuous over time, which is positive to the dense development of the microstructure.

The content of MSWIFA can significantly affect the activation process of GBFS. The formation of ettringite is accelerated by the increase in MSWIFA content in the early period, whereas the generation of Friedel's salt is inhibited in the high MSWIFA content. In the later period, the accumulation of C-(A)-S-H is enhanced by the increase in MSWIFA content. However, the rapid accumulation of ettringite in the early period and the large particle size of MSWIFA resulted in the large porosity and high harmful pore volume in high MSWIFA content.

In summary, the activation process of GBFS by MSWIFA is as follows: (i) The sulfate in MSWIFA can participate in the formation of ettringite, (ii) The chloride ions tend to generate Friedel's salt, (iii) The heavy metals ions in MSWIFA would be transformed into hydroxide precipitation, in the high alkalinity condition, (iv) The calcium ions, Si-O tetrahedral groups, and Al-O tetrahedral groups are polymerized as C-(A)-S-H gel. The harmful substances in the MSWIFA-activated GBFS system are effectively solidified. The chloride ions mainly participate in the generation of Friedel's salt. The heavy metals are transformed into hydroxide precipitation, are adsorbed by C-(A)-S-H, and further are covered by the compact microstructure.

4. Conclusion

In this study, the alkaline activating capability of MSWIFA was systematically investigated, and the macro performance and activation mechanisms of the new binder were comprehensively analyzed. The key findings are as follows:

(1) The MSWIFA-activated AAM system demonstrates a slow setting process, with continuously developing compressive strength and increasing pH over time. At 28 d, a compressive strength of 36.4 MPa is achieved with a 20 % MSWIFA and 80 % GBFS blend, highlighting the potential of this system as a sustainable cementitious material composed entirely of solid waste.

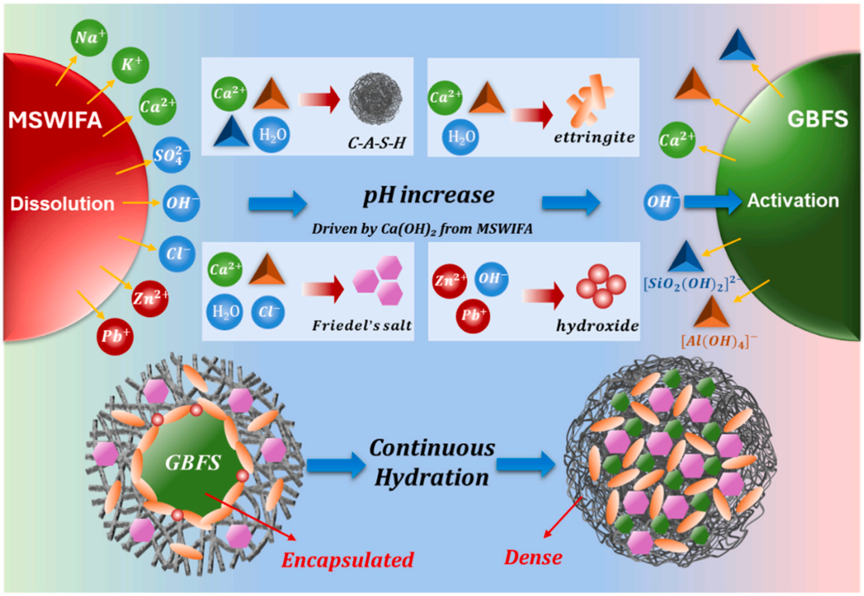

Fig. 11. The reaction mechanism of MSWIFA-activated GBFS system.

(2) The primary hydration products in the MSWIFA-activated system include ettringite, Friedel's salt, and C-(A)-S-H. In the early stages, the formation of ettringite, along with the precipitation of heavy metals, contributes to a prolonged induction period. Additionally, the presence of ettringite inhibits the formation of Friedel's salt. Over time, the accumulation of C-(A)-S-H plays a crucial role in enhancing the compressive strength of the material.

(3) While increasing the MSWIFA content promotes the formation of hydration products, a higher content of MSWIFA leads to increased porosity and a rise in harmful pore volume due to the larger particle size of MSWIFA. Moreover, the generation of Friedel's salt is hindered by the presence of ettringite, particularly at higher MSWIFA concentrations.

(4) The MSWIFA-activated GBFS system exhibits excellent environmental safety. Chloride ions are immobilized through their involvement in Friedel's salt formation, and heavy metals are effectively stabilized via precipitation reactions and physical adsorption. The leaching concentrations of heavy metals are well below the permissible limits set by national environmental standards, underscoring the system's environmental viability.

In sum, MSWIFA presents significant potential to activate other waste into a novel low-carbon cementitious material, utilizing solid waste while maintaining environmental safety and mechanical performance. The workability of the system has not yet been thoroughly investigated or optimized, and its practical applicability remains insufficiently explored. Future research should focus on a detailed analysis of the system's working performance and fluidity, as well as the influence of different curing methods on its properties. Additionally, further studies could examine the variability in performance of MSWIFA samples sourced from different regions.

CRediT authorship contribution statement

Yuzhe Li: Resources, Investigation, Data curation. **Junjie Zhang:** Writing – original draft, Project administration, Funding acquisition, Formal analysis, Conceptualization. **Yubin Cao:** Writing – review & editing, Resources, Funding acquisition, Data curation. **Yanru Wang:** Writing – review & editing, Validation, Software, Funding acquisition, Formal analysis. **Arezou Babaahmadi:** Writing – review & editing, Validation, Methodology. **Baodong Li:** Writing – review & editing, Visualization, Validation, Software. **Hao Wang:** Writing – review & editing, Validation, Methodology.

Declaration of Generative AI and AI-assisted technologies in the writing process

During the preparation of this work the authors used Chat GPT in order to improve the language of this paper. After using this tool, the authors reviewed and edited the content as needed and take full responsibility for the content of the published article.

Declaration of Competing Interest

The authors declare that they have no known competing financial interests or personal relationships that could have appeared to influence the work reported in this paper.

Acknowledgments

Natural Science Foundation from Shaanxi Province (2024JC-YBQN-0388), Taishan Scholar Programme of Shandong Province (tsqn202408222) and project 2025HWYQ-066 supported by Shandong Provincial Natural Science Fund for Excellent Young Fund Scientists Program (overseas) were gratefully acknowledged. The authors also acknowledge the financial support received from National Natural Science Foundation of China (Yanru Wang) and ARC-ITRH (Australian Research Council-Industrial Transformation Research Hub) research grant (IH200100010) allocated for Transformation of Reclaimed Waste Resources to Engineered Materials and Solutions for a Circular Economy (TREMS).

Data availability

Data will be made available on request.

References

[1] M. Jamalimoghadam, A.H. Vakili, I. Keskin, A. Totonchi, H. Bahmyari, Solidification and utilization of municipal solid waste incineration ashes: advancements in alkali-activated materials and stabilization techniques, a review, J. Environ. Manag. 367 (2024).
[2] J. Liu, G. Xie, Z. Wang, C. Zeng, X. Fan, Z. Li, J. Ren, F. Xing, W. Zhang, Manufacture of alkali-activated cementitious materials using municipal solid waste incineration (MSWI) ash: immobilization of heavy metals in MSWI Fly ash by MSWI bottom ash, Constr. Build. Mater. 392 (2023).
[3] X. Ma, T. He, Y. Da, Y. Xu, F. Zhao, Y. Sun, R. Yang, Improving the performance of incineration Fly ash as cement admixture by high-temperature sintering and its toxic leaching characteristics, J. Clean. Prod. 416 (2023).
[4] H.A. Ali, D. Xuan, B. Zhang, C. Xiao, B. Zhao, Cementitious characteristics and environmental behaviour of vitrified MSW incineration Fly ash slag, Clean. Mater. 4 (2022).
[5] C. Fan, Z. Wu, B. Wang, W. Zheng, Solidification of municipal solid waste incineration Fly ash with alkali-activated technology, J. Environ. Manag. 348 (2023).
[6] T. Li, B. Wang, X. Zhang, X. Han, Y. Xing, C. Fan, Z. Liu, Effect of nano silica on solidification/stabilization of heavy metal in alkali-activated MSWI Fly ash solidified body, Process Saf. Environ. Prot. 176 (2023) 462–474.
[7] W. Li, D. Yan, L. Li, Z. Wen, M. Liu, S. Lu, Q. Huang, Review of thermal treatments for the degradation of dioxins in municipal solid waste incineration Fly ash: proposing a suitable method for large-scale processing, Sci. Total Environ. 875 (2023) 162565.
[8] L. Su, S. Wu, G. Fu, W. Zhu, X. Zhang, B. Liang, Creep characterisation and microstructural analysis of municipal solid waste incineration Fly ash geopolymer backfill, Sci. Rep. 14 (1) (2024) 29828.
[9] J. Lan, Y. Dong, M.-F. Kai, H. Hou, J.-G. Dai, Investigation of waste alkali-activated cementing material using municipal solid waste incineration Fly ash and dravite as precursors: mechanisms, performance, and on-site application, J. Hazard. Mater. 465 (2024) 133416.
[10] J. Liu, Z. Wang, G. Xie, Z. Li, X. Fan, W. Zhang, F. Xing, L. Tang, J. Ren, Resource utilization of municipal solid waste incineration Fly ash - cement and alkali-activated cementitious materials: a review, Sci. Total Environ. 852 (2022).
[11] B. Ren, L. Chai, Y. Liu, R. Ma, Z. Liu, Y. Wang, Performance optimization design of high ductility cement-based alkali-activated municipal solid waste incineration Fly ash composite for rapid repair material, Constr. Build. Mater. 404 (2023).
[12] X. Xie, X. Liu, R. Liu, K. Lyu, Y. Zhu, J. Zuo, P. Zhang, C. Wu, S.P. Shah, Optimization formulation of low carbon MSWIFA cement-based composites modified by nano SiO2, J. Build. Eng. 80 (2023).
[13] J. Lan, Y. Dong, M.-F. Kai, H. Hou, J.-G. Dai, Investigation of waste alkali-activated cementing material using municipal solid waste incineration Fly ash and dravite as precursors: mechanisms, performance, and on-site application, J. Hazard. Mater. 465 (2024).
[14] C. Fan, W. Ding, B. Wang, Solidification/stabilization and optimization of municipal solid waste incineration Fly ash with aluminosilicate solid wastes, J. Environ. Manag. 357 (2024).
[15] Y. Xia, Z. Liu, Z. Song, R. Zhao, J. Wu, L. Wang, J. Yan, Valorization of municipal solid waste incineration Fly ash in low-carbon alkali-activated materials, Chem. Eng. J. 495 (2024).
[16] Y. Bai, W. Guo, J. Wang, Z. Xu, S. Wang, Q. Zhao, J. Zhou, Geopolymer bricks prepared by MSWI Fly ash and other solid wastes: moulding pressure and curing method optimisation, Chemosphere 307 (2022).
[17] Y. Bai, W. Guo, Y. Zhang, C. Xue, Z. Xu, Q. Gao, C. Xiao, Q. Zhao, Low carbon binder preparation from slag-red mud activated by MSWI Fly ash-carbide slag: hydration characteristics and heavy metals' solidification behavior, J. Clean. Prod. 374 (2022).
[18] J. Liu, J.-H. Doh, D.E.L. Ong, F.L. Kiely, Effect of thermal pretreatment on the reactivity of red mud valorized as aluminosilicate precursor for geopolymer production, Constr. Build. Mater. 445 (2024) 137943.
[19] S. Wang, Q. Zhao, W. Guo, C. Xue, Y. Bai, H. Pan, Y. Qiu, Preparation and characterization of mortar specimens based on municipal solid waste incineration Fly ash-activated slag, J. Build. Eng. 69 (2023).
[20] S. Wang, C. Xue, Q. Zhao, Y. Bai, W. Guo, Y. Shi, Y. Qiu, H. Pan, A novel binder prepared from municipal solid waste incineration Fly ash and phosphogypsum, J. Build. Eng. 71 (2023).
[21] P. Ren, T.-C. Ling, Roles of chlorine and sulphate in MSWIFA in GGBFS binder: hydration, mechanical properties and stabilization considerations, Environ. Pollut. 284 (2021).
[22] J. Liu, J.-H. Doh, D.E.L. Ong, H.L. Dinh, Z. Podolsky, G. Zi, Investigation on red mud and Fly ash-based geopolymer: quantification of reactive aluminosilicate and derivation of effective Si/Al molar ratio, J. Build. Eng. 71 (2023) 106559.
[23] L. Lang, M. Zhu, S. Pu, Recycling engineering sediment waste as sustainable subgrade material using ground granulated blast-furnace slag, electrolytic manganese residue and cement, Environ. Technol. Innov. 37 (2025) 103969.
[24] Y. Zuo, M. Nedeljković, G. Ye, Pore solution composition of alkali-activated slag/Fly ash pastes, Cem. Concr. Res. 115 (2019) 230–250.
[25] J. Zhang, Y. Li, G. Zhang, G. Li, A novel low-carbon binder: utilization of municipal solid waste incineration Fly ash and flue gas desulfurization gypsum to co-activate granulated blast furnace slag, Constr. Build. Mater. 472 (2025) 140963.
[26] M. Hongqiang, C. Hongyu, Z. Hongguang, S. yangyang, N. Yadong, H. Qingjie, H. Zetao, Study on the drying shrinkage of alkali-activated coal gangue-slag mortar and its mechanisms, Constr. Build. Mater. 225 (2019) 204–213.
[27] J. Zhang, H. Tan, M. Bao, X. Liu, Z. Luo, P. Wang, Low carbon cementitious materials: sodium sulfate activated ultra-fine slag/Fly ash blends at ambient temperature, J. Clean. Prod. 280 (2021) 124363.
[28] J. Zhang, C. Ye, H. Tan, X. Liu, Potential application of portland cement-sulfoaluminate cement system in precast concrete cured under ambient temperature, Constr. Build. Mater. 251 (2020) 118869.
[29] X. Liu, B. Ma, H. Tan, T. Zhang, J. Mei, H. Qi, P. Chen, J. Wang, Effects of colloidal nano-SiO2 on the immobilization of chloride ions in cement-Fly ash system, Cem. Concr. Compos 110 (2020) 103596.
[30] J. Wang, H. Tan, X. He, J. Zhang, S. Jian, C. Du, X. Deng, Influence of wet grinded slag on the hydration of phosphogypsum-slag based cement and its application in backfill tailings, Constr. Build. Mater. 360 (2022).
[31] N. Shao, X. Wei, M. Monasterio, Z. Dong, Z. Zhang, Performance and mechanism of mold-pressing alkali-activated material from MSWI Fly ash for its heavy metals solidification, Waste Manag. 126 (2021) 747–753.

[32] B. Qu, T. Liu, L. Duan, C. Gong, W. Luo, C. He, Y. Lv, The effect of sodium citrate on NaOH-activated BFS cement: hydration, mechanical property, and micro/nanostructure, Cem. Concr. Compos 133 (2022).
[33] H. Tan, X. Deng, X. He, J. Zhang, X. Zhang, Y. Su, J. Yang, Compressive strength and hydration process of wet-grinded granulated blast-furnace slag activated by sodium sulfate and sodium carbonate, Cem. Concr. Compos 97 (2019) 387–398.
[34] H. Sun, J. Qian, Y. Yang, C. Fan, Y. Yue, Optimization of gypsum and slag contents in blended cement containing slag, Cem. Concr. Compos 112 (2020) 103674.
[35] Y. Wang, L. Xu, X. He, Y. Su, W. Miao, B. Strnadel, X. Huang, Hydration and rheology of activated ultra-fine ground granulated blast furnace slag with carbide slag and anhydrous phosphogypsum, Cem. Concr. Compos 133 (2022).
[36] Y. Wang, X. He, Y. Su, H. Tan, J. Yang, M. Lan, M. Ma, B. Strnadel, Self-hydration characteristics of ground granulated blast-furnace slag (GGBFS) by wet-grinding treatment, Constr. Build. Mater. 167 (2018) 96–105.
[37] J. Zhang, H. Tan, L. Cai, X. He, W. Yang, X. Liu, Ultra-fine slag activated by sodium carbonate at ambient temperature, Constr. Build. Mater. 264 (2020) 120695.
[38] M. Niu, G. Li, Y. Wang, Q. Li, L. Han, Z. Song, Comparative study of immobilization and mechanical properties of sulfoaluminate cement and ordinary portland cement with different heavy metals, Constr. Build. Mater. 193 (2018) 332–343.
[39] J. Zhang, G. Li, W. Ye, Y. Chang, Q. Liu, Z. Song, Effects of ordinary portland cement on the early properties and hydration of calcium sulfoaluminate cement, Constr. Build. Mater. 186 (2018) 1144–1153.
[40] B. Wang, W. Ding, C. Fan, F. Liu, Immobilization properties and reaction mechanism of municipal solid waste incineration Fly ash with alkali activation technology, J. Build. Eng. 91 (2024).
[41] S. Wang, H. Pan, C. Xiao, Q. Zhao, J. Wang, Preparation and mix proportion optimization of red mud-Fly ash-based cementitious material synergistic activated by carbide slag and MSWIFA, Constr. Build. Mater. 415 (2024).
[42] B. Chen, B. Liu, L. Yang, S. Zaland, H. Ye, Solidification of heavy metal in municipal solid waste incineration Fly ash and performance evolution of alkali-activated foam concrete, Process Saf. Environ. Prot. 190 (2024) 850–862.
[43] J. Yang, L.H. Zeng, X.Y. He, Y. Su, Y.B. Li, H.B. Tan, B. Jiang, H.J. Zhu, S.K. Oh, Improving durability of heat-cured high volume Fly ash cement mortar by wet-grinding activation, Constr. Build. Mater. 289 (2021).
[44] J. Yang, F. Wang, Z. Liu, Y. Liu, S. Hu, Early-state water migration characteristics of superabsorbent polymers in cement pastes, Cem. Concr. Res. 118 (2019) 25–37.
[45] J. Yang, J. Huang, Y. Su, X. He, H. Tan, W. Yang, B. Strnadel, Eco-friendly treatment of low-calcium coal Fly ash for high pozzolanic reactivity: a step towards waste utilization in sustainable building material, J. Clean. Prod. 238 (2019) 117962.
[46] Y. Xia, Z. Liu, Z. Song, R. Zhao, J. Wu, L. Wang, J. Yan, Valorization of municipal solid waste incineration Fly ash in low-carbon alkali-activated materials, Chem. Eng. J. 495 (2024) 153577.
[47] J. Ren, B. Liu, J. Guo, J. Liu, F. Xing, H. Zhu, L. Zhao, T. Mi, Bio-treatment of municipal solid waste incineration Fly ash: a sustainable path for recyclability, J. Clean. Prod. 434 (2024).
[48] M. Niu, G. Li, L. Cao, X. Wang, W. Wang, Preparation of sulphate aluminate cement amended bentonite and its use in heavy metal adsorption, J. Clean. Prod. 256 (2020) 120700.
[49] G.R. Qian, J. Shi, Y.L. Cao, Y.F. Xu, P.C. Chui, Properties of MSW Fly ash-calcium sulfoaluminate cement matrix and stabilization/solidification on heavy metals, J. Hazard. Mater. 152 (1) (2008) 196–203.
[50] C. Xue, W. Zhang, Q. Zhao, The role of Al2O3, MgO and CaO in promoting Cl- uptake by hydrotalcite-like phases in alkali-activated binders with MSWI FA, Constr. Build. Mater. 439 (2024).
[51] X. Liu, X. Xie, R. Liu, K. Lyu, X. Wang, J. Yu, F. Fu, C. Wu, J. Zuo, Manufacture of alkali-activated cementitious materials using municipal solid waste incineration Fly ash (MSWIFA): the effect of the Si/Al molar ratio on fresh and hardened properties, Constr. Build. Mater. 409 (2023).
[52] K. Shiota, T. Nakamura, M. Takaoka, S.F. Aminuddin, K. Oshita, T. Fujimori, Stabilization of lead in an alkali-activated municipal solid waste incineration Fly ash–Pyrophyllite-based system, J. Environ. Manag. 201 (2017) 327–334.
[53] L. Guo, X. Xu, Q. Wang, J. Park, H. Lei, L. Zhou, X. Wang, Machine learning-based prediction of heavy metal immobilization rate in the solidification/stabilization of municipal solid waste incineration Fly ash (MSWIFA) by geopolymers, J. Hazard. Mater. 467 (2024).
[54] J. Liu, L. Hu, L.P. Tang, J. Ren, Utilisation of municipal solid waste incinerator (MSWI) fl y ash with metakaolin for preparation of alkali-activated cementitious material, J. Hazard. Mater. 402 (2021).
[55] J. Zhang, H. Tan, X. He, W. Yang, X. Deng, Utilization of carbide slag-granulated blast furnace slag system by wet grinding as low carbon cementitious materials, Constr. Build. Mater. 249 (2020) 118763.
[56] J. Zhang, Y. Li, G. Zhang, G. Li, A novel low-carbon binder: utilization of municipal solid waste incineration Fly ash and flue gas desulfurization gypsum to co-activate granulated blast furnace slag, Constr. Build. Mater. 472 (2025).